Nuclear Transparency of Photoproduced ρ^0 Mesons

Bhesha Raj Devkota
Department of Physics & Astronomy
Mississippi State University
Mississippi State, MS

April 2024

TABLE OF CONTENTS

CHAPTER

CHAPTER I

INTRODUCTION

1.1 Introduction

Most of the visible matter consists of protons, neutrons, and electrons, which are governed by different fundamental forces. These underlying forces of nature, namely strong nuclear, electromagnetic, weak nuclear, and gravitational forces have been researched extensively and the first three are well portrayed within the Standard Model.

Strong interaction's response at low energies is explained in the context of nucleons exchanging mesons [19]. In contrast, perturbative Quantum Chromodynamics (pQCD) describes strong interactions at high energies taking into consideration quarks and gluons. Although the explanation of the strong force can be understood using two distinct theories at low and high energies, the transition from the low-energy scale to the high-energy scale has not been definitively established. Color transparency (CT), a key prediction of Quantum Chromo Dynamics (QCD) is used to investigate this transition from nuclear-meson degree of freedom to that of quark-gluon degree of freedom. QCD-inspired calculations anticipate the decrease in the final state interaction between hadrons and nuclear medium when subjected to the large momentum transfers [18]. This contradicts the conventional nuclear physics calculation which was based upon Glauber multiple scattering theory [28] which assumes there is a strong initial and final state interaction as well as rescattering and is independent of energy and momentum transfer.

Pioneered by Brodsky and Mueller [37] in the framework of pQCD, CT was later demonstrated to also arise in non-perturbative models [26]. The prediction of CT is based on three distinct phenomena: squeezing, freezing, and reduced interaction. First, when a high momentum transfer occurs during scattering, there exists a tendency to favor amplitudes associated with initial state as well as final state hadrons possessing a compact transverse size. This small compact size configuration (squeezing), often known as Point-like configuration(PLC) is much smaller in size compared to that of a hadron. Secondly, this PLC should not radiate any gluon and must be color-neutral outside of its radius. Its small size and color neutrality make it interact less with the surrounding hadrons resulting in color screening. Finally, this leads to the continuation of no further interaction with the nuclear medium(freezing). Freezing is due to time dilation which makes the PLC stay small long enough to cross the nucleus before it returns to its regular size. This freezing process is supposed to be governed by energy transfers, whereas the squeezing phenomenon is supposed to be controlled by momentum transfers [23].

Nuclear Transparency (T), the measurable quantity to search for the onset of Color transparency is mathematically described as the ratio of cross-sectional area per nucleon for a procedure involving a bound nucleon within a nucleus compared to that of an unbound nucleon. The increase in Nuclear Transparency signifies the onset of the CT. Hence, lots of researchers have been dedicated to measuring nuclear transparency for the past three decades to understand CT phenomenon. A sign of the onset of CT means there should be a positive increase in the slope of nuclear transparency with regard to momentum transfers [23]. The combined effect of freezing and squeezing plays an important role in raising nuclear transparency concerning energy or momentum transfers. Thus, the observation of squeezing and freezing is essential to look for Color Transparency.

Most previous experiments of Nuclear transparency have been conducted with electron or hadron scattering. Photonuclear is an alternative way to study Nuclear transparency. Photonuclear reactions offer valuable insights into several aspects of nuclear structure, offering an additional perspective compared to quasi-elastic proton knockout and electron scattering experiments. The photon shows different characteristics depending on the momentum transfer: It is typically described as a vector-meson state at low momentum transfers and a point-like particle at high momentum transfers. However, the transition between this state has never been mapped before. Successful extraction of nuclear transparency will provide crucial insight into photon structure and the onset of CT. We aim to seek an answer on three [31] fundamental aspects of QCD.

1. Determining the momentum transfer t, at which the transition of the photon from vector meson to that of point-like configuration can be established.

2. Identifying the momentum transfer t at which the onset of CT occurs in hadrons.

3. To understand and accurately explain the differences in nuclear transparency of various mesons.

1.2 Previous Experiments

From the late 20th century attempts to understand CT phenomena led to numerous experiments on baryons and mesons. The initial efforts to understand the onset of CT were carried out by Brookhaven National Lab (BNL) using proton knock-out reactions at intermediate energies [20, 34, 32, 9] involving hydrogen along with various nuclear material as a target across incident proton momenta ranging from 6 to 12 GeV. These experiments show an energy-dependent transparency, where transparency was observed to have a positive increase between 6-9.5 GeV and a sudden

decrease between 9.5-14.4 GeV. This phenomenon is not currently identified as CT. Possible explanations for the fall in transparency at high momenta can be correlated to nuclear filtering [30] or the threshold of charmed quark resonances [17]. This scenario casts uncertainty on our capacity to understand CT using proton-induced knockout reactions.

Additional experiments on baryons were conducted at Jefferson Lab [8, 27, 15] and Stanford Linear Accelerator Center(SLAC) [33, 38] using $A(e, e', p)$ reactions. Weak electromagnetic probes are simpler than the hadronic probes such as protons. This simplicity arises because a comprehensive understanding of momentum distribution and nuclear energy within various nuclei has been derived through extensive measurements of low energy $A(e, e', p)$ reactions. No significant onset of CT has been observed for $Q^2 \approx$ 2-14.2 GeV^2. Nuclear transparency extracted from these experiments on baryons using weak electromagnetic reactions corresponds with traditional physics calculation and they don't support the onset of CT from $Q^2 \approx$ 2-14.2 GeV^2.

Experiment conducted on mesons however gives promising results at both high and moderate energies. In comparison to the three quark systems, it is easier to produce a small-size configuration for the quark-anti-quark system. In this context, CT's onset in mesons is anticipated to take place at energies lower than those associated with baryons [16]. Furthermore, The $A(e, e'\pi^+)$ reaction at JLAB [21, 42] distinctly indicates CT's onset for pion mesons. Moreover, findings from the CLAS Collaboration on incoherent ρ mesons production at fixed coherence length indicate the onset of CT [25].

The $(\gamma + n \rightarrow \pi^- + p)$ on helium nuclei [24] was the first experiment to seek for the onset of CT employing photo-production. The figure 1.1 shows the Nuclear transparency obtained from ^4He target.

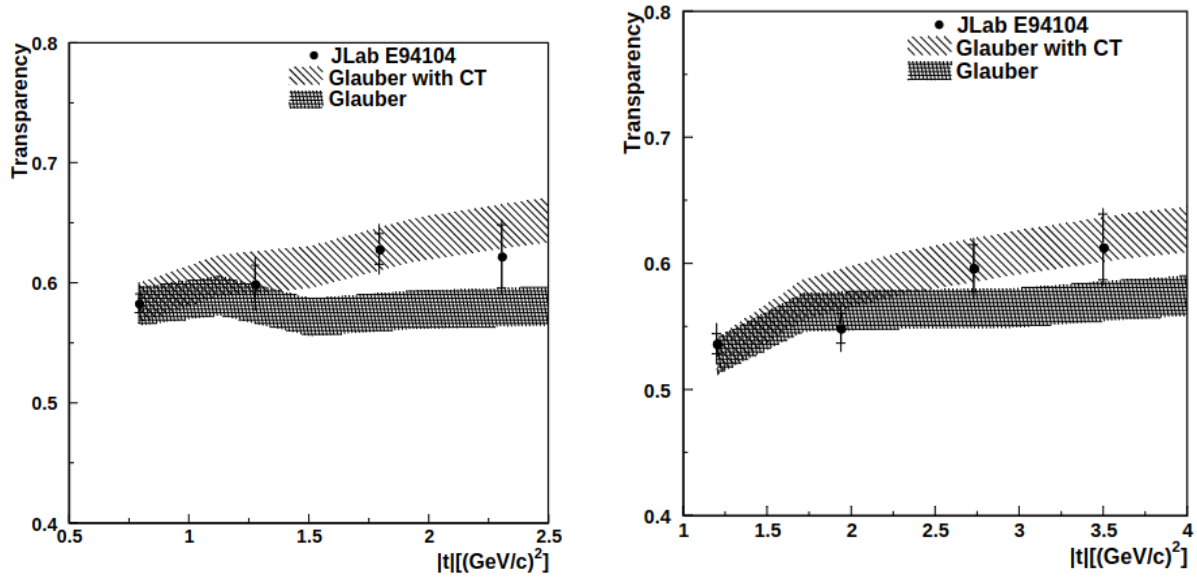

Figure 1.1: Nuclear Transparency of ^{4}He(γ, p, π^-) at $\theta^{\pi}_{\rm cm} = 70°$ and $90°$ vs momentum transfer $|t|$. The internal error bars denote statistical uncertainties, while the outer error bars correspond to the combination of statistical and point-to-point systematic uncertainties, added together in quadrature, [24].

1.3 The SRC-CT Experiment

One of the goals of Experiment E12-19-003 [35] is to study photo nuclear transparency varying with high momentum transfers over different nuclei targets. A key aspect of the photo-nuclear reaction in Hall D Jefferson Lab is that, without changing the momentum transfer, complete energy transfer can proceed in a reaction. This guarantees adequate freezing of the expansion times even for modest momentum transfers which are necessary to observe for CT. The High luminosity of the GlueX detector [10], combined with a tagged photon beam and good acceptance, allowed large-angle photo nuclear scattering to be measured. This process produces baryons and mesons. According to Ref [31] at large momentum transfer CT effects can be observed over a wide distribution of $|t|$ and center-of-mass angle using GlueX in Hall D at Jefferson lab. It can be observed for a tagged photon beam with beam energy between 6-10 GeV.

1.4 Detector

The schematic representation of the GlueX detector and beamline configuration is shown in Figure 1.2. The experimental Hall D at Jefferson Lab relies on the 12 GeV electron beam provided by the Continuous Electron Beam Accelerator Facility (CEBAF). Coherent bremsstrahlung [43] off a 50 μm diamond radiator produces linearly polarised beam photons, with coherent beam energy of 8.8 GeV. The Tagger Hodoscope and Tagger microscope [45] are used to determine the energy of photons. These beam photons are then directed towards various targets including 30 cm long liquid helium and liquid deuterium targets, as well as 8 equidistant multi-foil carbon targets measuring 30 cm in length and 1.9 cm in thickness. Electrons that do not interact with the radiator are directed to an electron beam dump. The linear polarization of the photons is measured by a triplet polarimeter [22], while the flux is measured by a Pair Spectrometer [13].

The GlueX spectrometer is built within a 4-meter-long 2T superconducting magnet [12]. The target is surrounded by the scintillator-based start counter (SC) [41] to help in selecting the correct beam bunches, and the center and forward drift chamber (CDC [29] and FDC [40]) for tracking charged particles. The chambers can track protons with momentum as low as 0.25 GeV. Further downstream, the time of flight (TOF) [39] system measures the flight time of charged particles. Photons are detected by Barrel calorimeter (BCAL) [14] located inside the solenoid, while Forward calorimeter (FCAL) [36] downstream to TOF, is used for additional photons measurement. TOF measurements and energy loss recorded by the CDC are used for particle identification. Further details regarding the working of the GlueX detectors can be found in Ref [10].

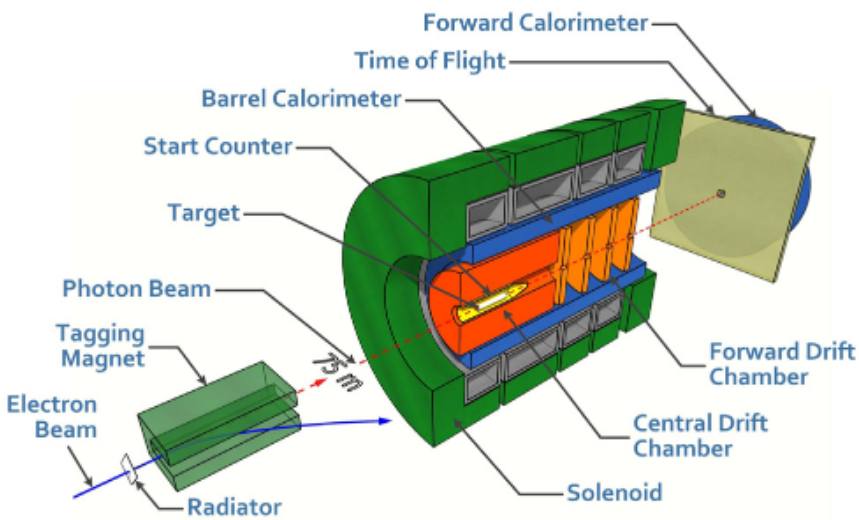

Figure 1.2: A schematic representation of GlueX detector in Hall D [10].

CHAPTER II

EVENT SELECTION

2.1 Overview

We studied the reactions $(\gamma, \pi^+\pi^- p)\mathbf{X}$ to detect events produced from the photo-production of ρ^0 mesons where the final states, ρ^0 mesons subsequently decay into π^+ and π^- [44]. Our dataset includes data collected during the SRC-CT experiments conducted over 45 days between November and December 2021 using three different target materials: deuterium, helium, and carbon.

Our Analysis workflow depends on the computing framework developed by the GlueX Collaboration. The experiment used CEBAF online data acquisition (CODA) system to collect data which is stored in the evio file format [3]. Later, a subset of this raw data went through detector calibrations, and the resultant calibration constants were stored in the Calibration Constant Data Base (CCDB) [6]. Utilizing these calibration constants, we used the standard GlueX **halld_recon**[1] software to reconstruct the data in Reconstructed Event Storage (REST) file format. We used the ver01 REST file, which includes all of the kinematic details of the event of interest. The size of the REST file was enormous to work on, so they were then processed using the standard GlueX ReactionFilter plugin to generate output analysis trees of reduced size. These analysis trees were further skimmed using the DSelector [7] macro. Throughout these processes, the file size remained sufficiently small for analysis, paving the way for the physics exploration.

[1] https://github.com/JeffersonLab/halld_recon/wiki

2.2 Selection using ReactionFilter

We used the reaction filter plugin [1] to study the final state composition of $(\pi^+\pi^- p)\mathbf{X}$ where $\mathbf{X}$ represents the missing unknown particle. Our reaction of interest was based on a hypothesis in which we would detect two tracks of positive charge and one track of negative charge, out of which the two positively charged tracks are candidates for a proton and a π^+, while the negatively charged track is a candidate for a π^-. At this stage, two extra tracks were added, with the number of showers limited to five to reduce additional hadronic showers originating from photons. It was required to have a common vertex for tracks and to conserve four-momentum. Additionally, four additional beam bunches on each side were recorded to subtract accidental beam photons.

The Reaction Filter implemented sets of loose particle identification selection cuts using the detector's timing and energy loss information for common particles that produced well-understood and distinct patterns. Further details about this standard Gluex Particle identification cuts can be found in Ref. [2]. The output root file was saved into Physics Analysis Root Tree (PART) [4]. This hypothesis was repeated for all of our targets. The version of our database is shown in Table 2.1 alongside associated PART trees.

The basic PID timing and energy loss dE/dx cuts applied at the reaction filter to identify π^+, π^-, and proton candidates for our hypothesis are listed in the table below(Table 2.2 and Table 2.3). The time of flight timing distribution of π^+ candidate, both before and after applying the cut as listed in Table 2.2, is shown in Figure 2.1. Additionally, the distribution of energy loss vs momentum of proton candidates before and after applying the cut as listed in Table 2.3 is shown in Figure 2.2. The curve at the upper region corresponds to proton and the curve at the flat region corresponds to pions. It is because at low momentum protons loose energy faster to that of pions.

S.N	Target	REST	Analysis	PART Trees
1	Deuterium	ver01	ver06	tree_gd_pippimprotinc__B4_F4_T2_S5
2	Helium	ver01	ver06	tree_ghe_pippimprotinc__B4_F4_T2_S5
3	Carbon	ver01	ver06	tree_gc12_pippimprotinc__B4_F4_T2_S5

Table 2.1: Target, REST, and analysis version along with output analysis tree from ReactionFilter plugin. Flag B4, F4, T2, and S5 are used in the PART Trees. B4 means there are four beam bunches on each side of the main signal peak. F4 stands for applying constraints on both the vertex as well as the four-momentum. T2 represents two extra tracks and S5 represents the number of extra showers limited to 5.

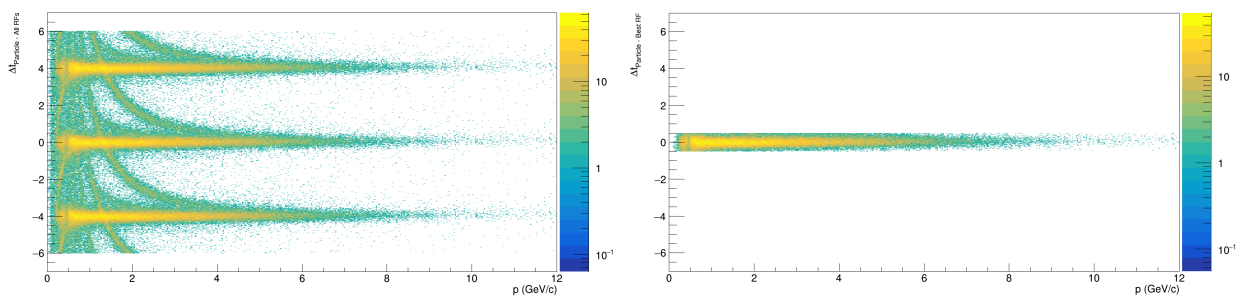

Figure 2.1: Timing of TOF detector vs. π^+ candidate momentum both before and after applying the time cut listed in Table 2.2.

2.3 Selection using DSelector

The PART root files obtained from reaction filter plugins were further processed using DSelector software. Our analysis represents three distinct reactions for the $\gamma d \to \pi^+\pi^- p\ (X)$, $\gamma\,^4\mathrm{He} \to \pi^+\pi^- p\ (X)$, and $\gamma\,^{12}\mathrm{C} \to \pi^+\pi^- p\ (X)$ final state. Regardless of the target material, the selection criteria

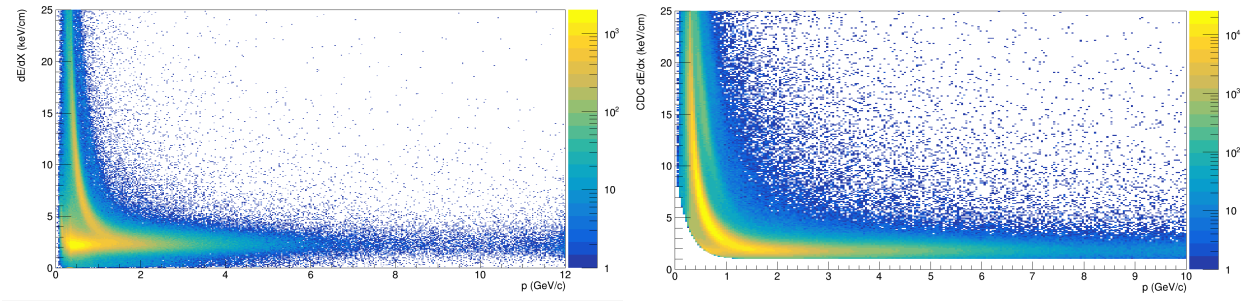

Figure 2.2: 2D plots of dE/dx vs momentum of proton candidate before and after applying cut on energy loss of dE/dx listed in Table 2.3. The plots in this figure are only for demonstrated purposes. The left plot is data with fewer events while the right plot is data for one full run period. dE/dx cuts helps identifying particle with momentum less than 1 GeV.

Particle ID	**Timing Offset**			
	BCAL/RF	**TOF/RF**	**FCAL/RF**	**SC/RF**
Charged Pions	± 1.0 ns	± 0.5 ns	± 2.0 ns	± 2.5 ns
Protons	± 1.0 ns	± 0.6 ns	± 2.0 ns	± 2.5 ns

Table 2.2: Timing offsets applied on RF based on particle type and detector.

Particle ID	**CDC dE/dx Cut (keV/cm)**	**Combined dE/dx Cut (FDC,SC,TOF)**
Charged Pions	$(< 3 + \exp(-7\,\lvert\mathbf{p}\rvert) + 6.2$	Not applied
Protons	$(> 2.25 + \exp(-4\,\lvert\mathbf{p}\rvert) + 1$	Not applied

Table 2.3: Energy loss dE/dx cut criteria implemented in the Reaction Filter plugin.

applied to these reactions remained consistent. These criteria are summarized below in Table 2.4.

Name of Variable	**Selection Criteria**	**Subsection**
Kinfit Confidence Level	CL $>10^{-3}$	2.3.1.
Accidental	Background Subtraction	2.3.2.
Extra Tracks	Removal of additional tracks	2.3.3.
Beam Energy	$6.5 < E_\gamma < 10.8, GeV$	2.3.4.
Missing momentum	$P_{\text{miss}} < 300, MeV$	2.3.5.
Vertex	$52 < z < 78$ cm	2.3.6

Table 2.4: Event selection criteria in the DSelector stage for the $\gamma A \rightarrow \pi^+\pi^- p\ (X)$ reaction channel.

2.3.1 Kinfit Confidence Level

In our analysis, we impose several constraints on our hypothesis. Specifically, we require that the decaying pions originate from the common vertex indicating that they emerge from the same point in space. Additionally, we enforce the conservation of four-momentum and energy. These constraints are integrated into the kinematic fit algorithm, which optimizes to best fit the observable and assumes the final states of pions to originate from ρ^0 mesons. Detailed explanations of the kinematic fit used in the Standard GlueX algorithm can be found in Ref. [5]. The Kinematic Fit confidence level distribution is shown in Fig. 2.3. A flat distribution indicates well-fitted events

that have a higher confidence level near value one, while poorly-fitted events are clustered near zero and therefore rejected from our analysis.

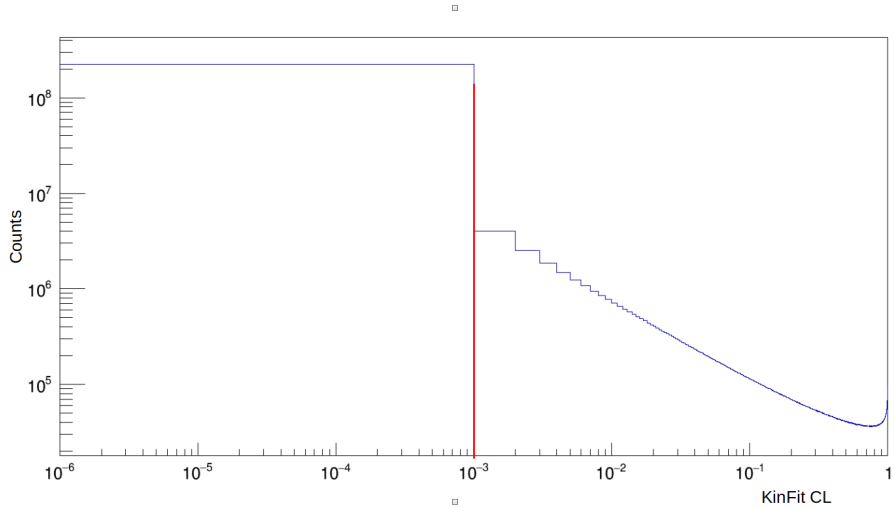

Figure 2.3: Kinematic Fit for the confidence level. Events with a confidence level below 10^{-3} are rejected as they indicate poor fits [5].

2.3.2 Accidental Background

CEBAF uses radio frequency pulses with a frequency of 1497 MHz to accelerate the electrons delivered to Hall D. The primary beam bucket is assigned to time = 0 and extends over a time interval of 4 ns. The center beam with a time interval of $[-2.004\text{ns}, 2.004\text{ns}]$ as shown in figure 2.4, is often called a prompt beam. Because of the high photon flux, and the limited resolution of the detector, the selection criteria for the beam photon can be accidentally matched by beam photons originating from RF bunches adjacent to the primary bunch. Some of these accidentally matched beam photons are recorded under the prompt peak. To remove these accidental photons under the prompt peak, we include four adjacent RF bunches on each side of the primary RF bunch

during the reaction filter stage, matching the timing of these wrong RF bunches having a 4 ns time interval. We subtracted the accidental beam photons from the prompt beam, and we selected two out-of-time beam buckets at ± 8.0 ns and ± 12.0 ns about the prompt peak and scaled them by the factor of -1/4. The beam photons before and after accidental subtraction are shown in Figure 2.4. Also, we prevented choosing out-of-time beams of ± 2.0 ns to prevent the effects of the tail of the prompt peak in these regions.

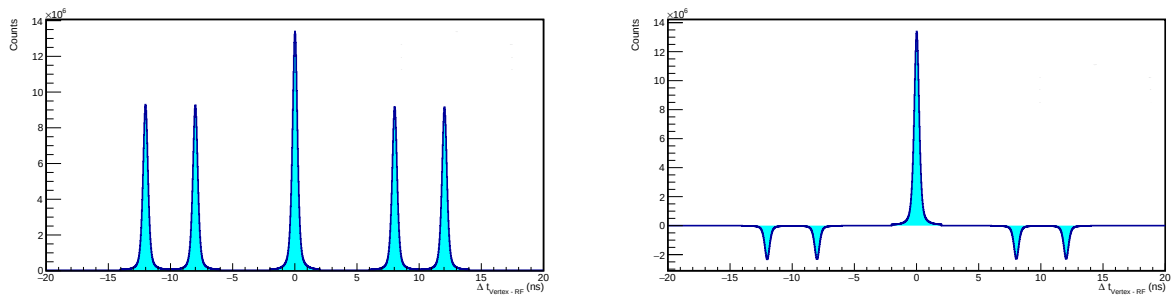

Figure 2.4: Distribution showing timing variation between RF and beam time. The plot on the left demonstrates this distribution before accidental subtraction, while the plot on the right illustrates it after accidental subtraction. The central peak represents a weight of 1, whereas the side peak is weighted as -1/4.

2.3.3 Cut on Extra Tracks

In exclusive reactions where all final particles are detected, keeping some extra tracks during the kinematic fit process can be helpful to mitigate the loss of some of the good signals. However, given our focus on nuclear targets, where a breakup is expected and only pions and protons are detected, keeping the extra tracks initiates unnecessary combinations of final states particles. We

chose to reject events with extra tracks. Pions at high momentum often interacted with detector materials to produce hadronic showers, which were crucial for reconstructing ρ^0 mesons. Thus, the cut on the number of showers was set at five. This ensured that we did not reject true signals.

2.3.4 Beam Energy

We required a beam energy greater than 6 GeV in Hall D to investigate the CT phenomena [31] and establish the transition of photons between point-like and vector meson states. Further, modeling luminosity at low energy levels is challenging. Therefore, for this analysis, our corresponding beam energy was

$$6.5 < E_\gamma < 10.8 GeV$$

This range ensured that we had the necessary energy for our study.

2.3.5 Missing momentum

In the reaction ($\gamma A \rightarrow \pi^+\pi^- p\mathbf{X}$), we defined missing four vector as $P_{\text{miss}} = (E_{\text{miss}}, \vec{p}_{\text{miss}})$, and it is calculated as:

$$P_{\text{miss}} = (P_{\pi^+} + P_{\pi^-} + P_p - P_\gamma)$$

where:

$$P_\gamma : \text{Four momentum of the photon beam,}$$

$$P_{\pi^+}, P_{\pi^-}, P_p : \text{Four momenta of detected final state particles.}$$

We are interested in events in the mean-field (MF) region and reject events originating from the Short-Range Correlation (SRC) region. For this we applied a selection cut on missing momentum $|\vec{p}_{\text{miss}}| < 300$ MeV as shown in Fig. 2.5.

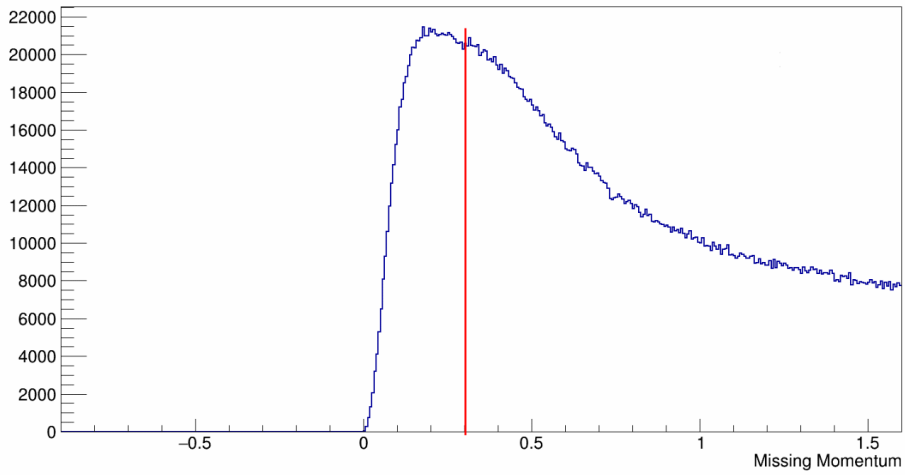

Figure 2.5: Missing Momentum distribution for Deuterium Events. We reject events with Missing Momentum >300 MeV

2.3.6 Cut on Vertex

To avoid the cell walls and the target window the GlueX Collaboration recommended a vertex cut of $52 < z < 78$ cm [11] as shown in Fig. 2.6

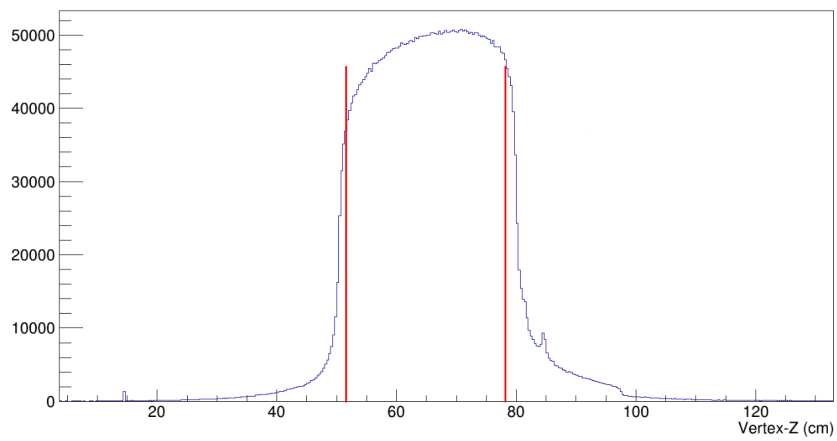

Figure 2.6: Vertex distribution for deuterium target where $52 < z < 78$ cm.

2.3.7 Cut on the Proton's Polar Angles

Most of the selection cuts were applied within the DSelector Stage. The output root file was saved as a Flat tree, where the surviving combos (one entry for each combination of beam plus final state particles) from all those analysis cuts were stored for further analysis. For the reaction ($\gamma A \rightarrow \pi^+\pi^- p\mathbf{X}$), we defined the Mandelstam variable $t = -(P_\gamma - P_{\pi^+\pi^-})$, where P_γ represents the four-vector of the incoming beam and $P_{\pi^+\pi^-}$ represents the four-vector of the $\pi^+\pi^-$ system. The analysis was carried out in six regions as shown in Table 2.5. Understanding the combinatorial

S.N	$\lvert -t \rvert GeV^2$ **range**
1	$1.0 < \lvert -t \rvert GeV^2 \leq 1.2$
2	$1.2 < \lvert -t \rvert GeV^2 \leq 1.4$
3	$1.4 < \lvert -t \rvert GeV^2 \leq 1.8$
4	$1.8 < \lvert -t \rvert GeV^2 \leq 2.6$
5	$2.6 < \lvert -t \rvert GeV^2 \leq 3.4$
6	$3.4 < \lvert -t \rvert GeV^2 \leq 4.6$

Table 2.5: Ranges of Mandelstam variable $\lvert -t \rvert$

background from mispairing of the pions and protons, such as the misidentification of pions and protons, particularly at high momentum transfers is essential. To address this, selection cuts were further applied by studying the simulated events using the Geant4 Simulation of GlueX Detector. These simulated events were subjected to the same criteria as those applied to measured data. This selection strategy aims to suppress background noise from signal events effectively. Currently,

work is ongoing to study the detailed background using the background event generator for the GlueX Detector - Bggen. The selection cuts will be further refined based on the simulated physical background. The following event selection cuts were used in the analysis.

The 2D distribution plots of the proton's polar angle and the invariant mass of $\pi^+\pi^-$ mesons for simulated events and measured data are shown in Figures 2.7, and 2.8 respectively. These plots are divided into different ranges of $|-t|GeV^2$ distribution as listed in Table 2.5.

From the simulated event as shown in Figure 2.7, it is clear that events with polar angles below 20 degrees likely originate from the combinatorial background. Similarly, the 2D distributions of the proton's polar angle and the invariant mass from measured data as shown in Figure 2.8, suggests that events below 20 degrees may result from multiple candidates of charged particles that passed the event-selection criteria. Based on these observations from both simulated and measured events, we establish selection criteria for the proton's polar angle. We selected events with polar angles greater than 25 degrees for $|-t| \leq 3.4GeV^2$, and those greater than 20 degrees for $3.4 < |-t|GeV^2 \leq 4.6GeV^2$.

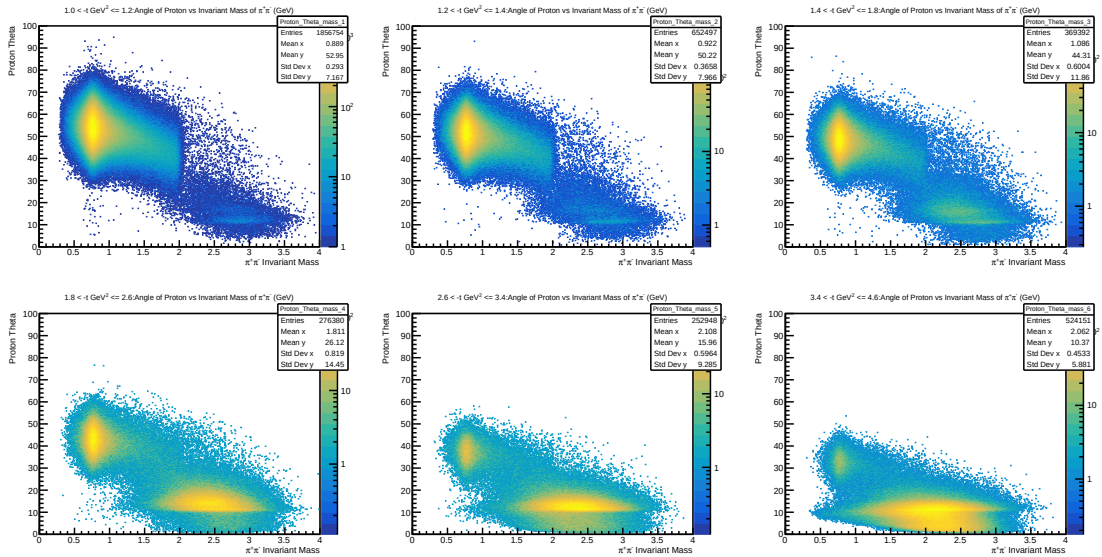

Figure 2.7: Distribution of Proton's polar angle for invariant mass for different binning in $|-t|GeV^2$ for Simulated events.

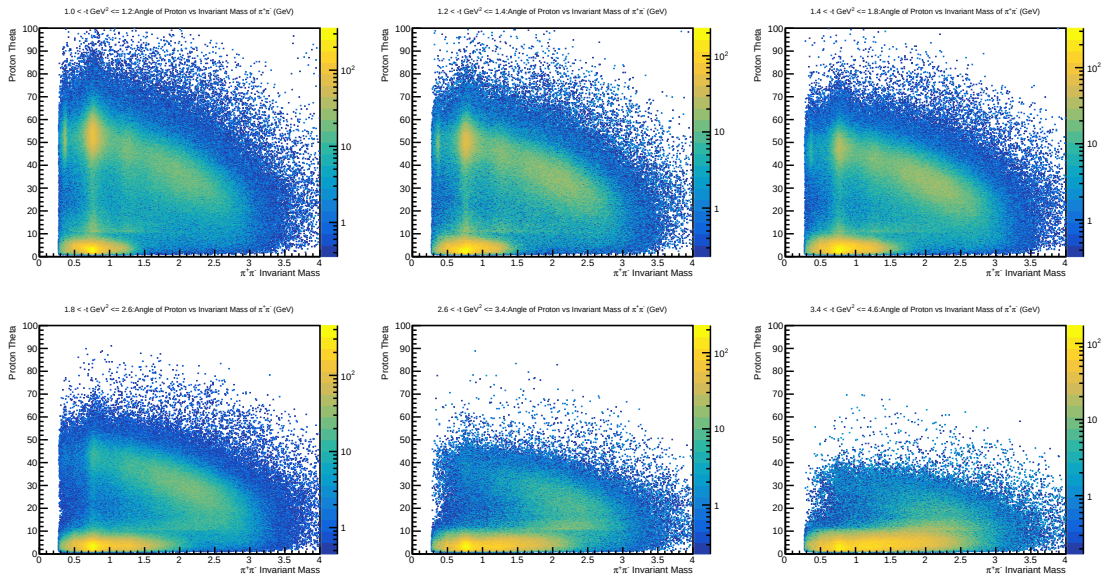

Figure 2.8: Distribution of Proton's polar angle for invariant mass for different binning in $|-t|GeV^2$ for Measured data.

CHAPTER III

PHYSICS ANALYSIS

The invariant mass distributions of simulated events for helium targets, both before and after applying the angular cuts on the proton candidate, as described in Section 2.3.7 are shown in Figure 3.1 and Figure 3.2 respectively. Additionally, Figure 3.3 shows the invariant mass distribution for measured helium data. Similar patterns are observed in the invariant mass distributions for deuterium and carbon. There is a notable peak at 0.37 GeV to the left of the ρ^0 meson peak in the invariant mass distribution. This corresponds to the $\phi(1010)$ meson decay into K^+K^- which is misidentified as pions, leading to the observed peak. Furthermore, the peak at 1.270 GeV is due to $f_2(1270)$ mesons decaying into $\pi^+\pi^-$.

3.1 Data Yield Extraction

The invariant mass distribution was fitted using a relativistic Breit-Wigner signal with a first-order polynomial, plus a Breit-Wigner background for $|-t|$ up to 2.6 GeV^2.For $|-t|$ values ranging from 2.6 to 4.6 GeV^2, a relativistic Breit-Wigner signal with a second-order polynomial was used. The resulting fit for deuterium, helium, and carbon targets with different bins in $|-t|$ are shown in Figures 3.4, 3.5, 3.6, respectively. Due to the reconstruction of $\phi(1010)$ meson as $\pi^+\pi^-$ distribution, a peak was observed at 0.37 GeV. As this peak is far from the ρ^0 signal peak, we chose not to include this region during the fitting process. The combined function was initially fitted

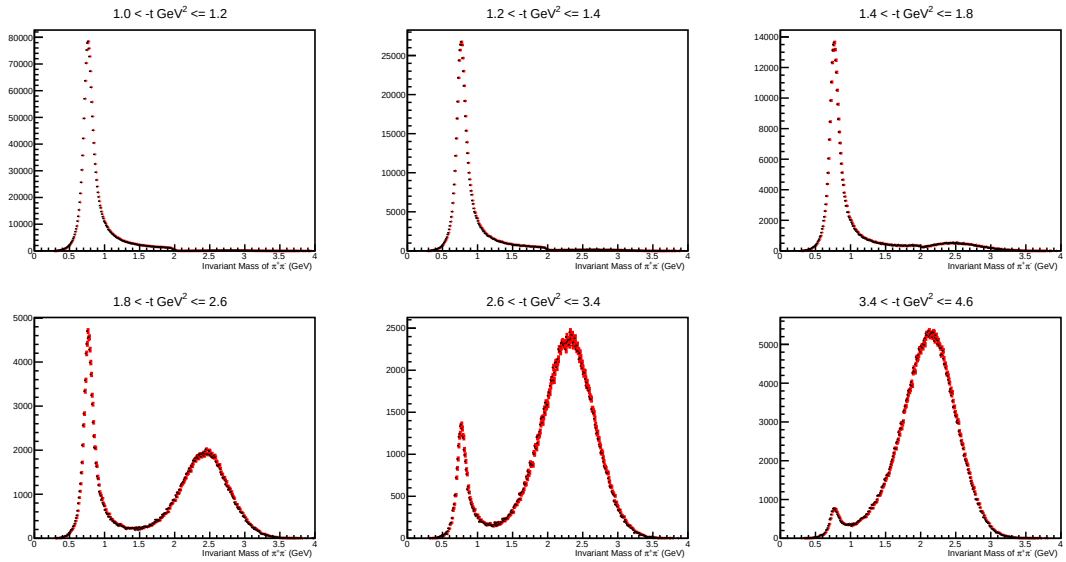

Figure 3.1: Invariant mass distribution of simulated events for helium targets before applying selection angular cuts on proton candidate.

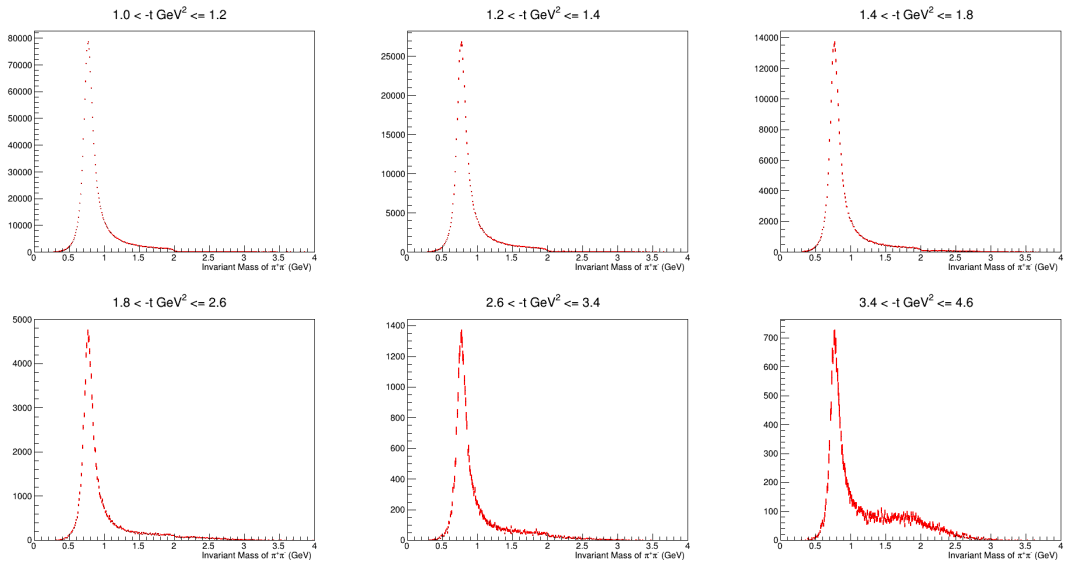

Figure 3.2: Invariant mass distribution of simulated events for helium targets after applying selection angular cuts on proton candidate.

using a combination of relativistic Breit-Wigner and polynomial functions. The signal function was then derived by subtracting the fitted background polynomial from the combined function. Both the signal yields and background yields were obtained by integrating the signal and background functions, respectively, over the range of $0.6 < M_{\pi^+\pi^-} < 0.92$. This range will be further refined in future studies.

3.1.1 Statistical Uncertainty in Yields

The error determination in data points in Figures 3.4, 3.5, 3.6 follows Poisson statistics. Let N_{total} represent a combined yield, and N_{bgd} represent the background yield. The statistical uncertainties on N_{total} and N_{bgd} are denoted by δN_{total} and δN_{bgd}, respectively. The signal yield is

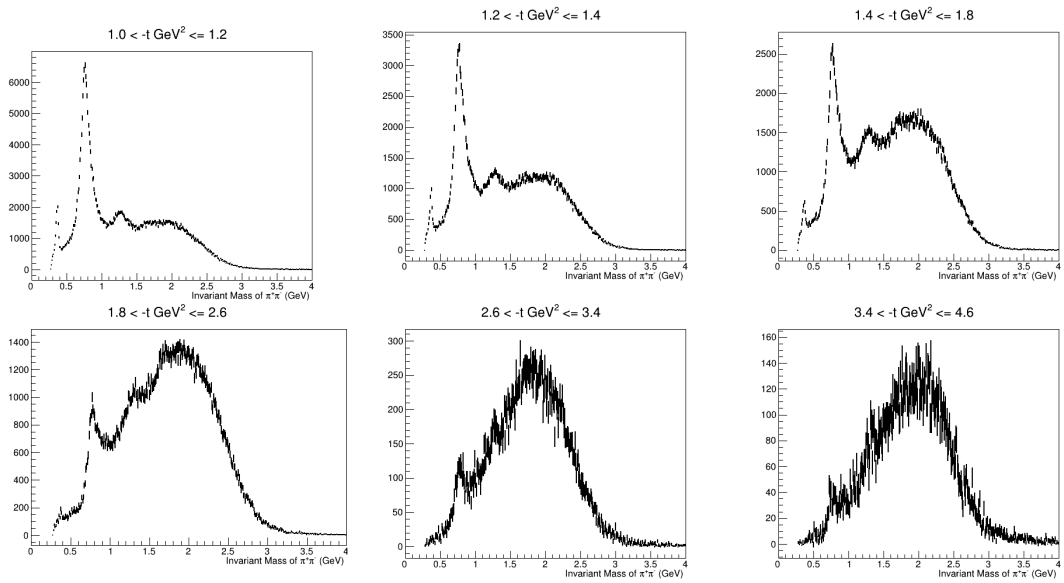

Figure 3.3: Final Invariant Mass distribution of $\pi^+\pi^-$ distribution after applying all selection criteria.

calculated as the difference between the combined signal (N_{total})and the background contribution N_{bgd}:

$$N_{signal} = N_{total} - N_{bgd}, \tag{3.1}$$

From error propagation, the error in signal yield is given by,

$$(\delta N_{signal})^2 = (\delta N_{total})^2 + (\delta N_{bgd})^2 \tag{3.2}$$

Following Poisson statistics, the variance of a variable K is given by the mean value of K. Therefore, the error in the signal yield in Eq. 3.2 can be written as,

$$(\delta N_{signal})^2 = N_{total} + N_{bgd}. \tag{3.3}$$

Substituting the total signal from Eq. 3.1in terms of the signal yield and background contributions to Eq. 3.3, the variance is

$$(\delta N_{signal})^2 = N_{signal} + 2N_{bgd}. \tag{3.4}$$

The variance is thus given as the yield plus twice the background contribution. We calculated the uncertainty in the signal yield using the equation

$$\sqrt{(N_{signal} + 2N_{bgd})} \tag{3.5}$$

These calculated yields for deuterium, helium, and carbon targets are summarized below in Table 3.1.

3.2 Efficiency

Efficiency was determined using Monte Carlo simulation. A mean-field simulation for all three nuclei was utilized to generate the invariant mass distributions. The invariant mass distribution

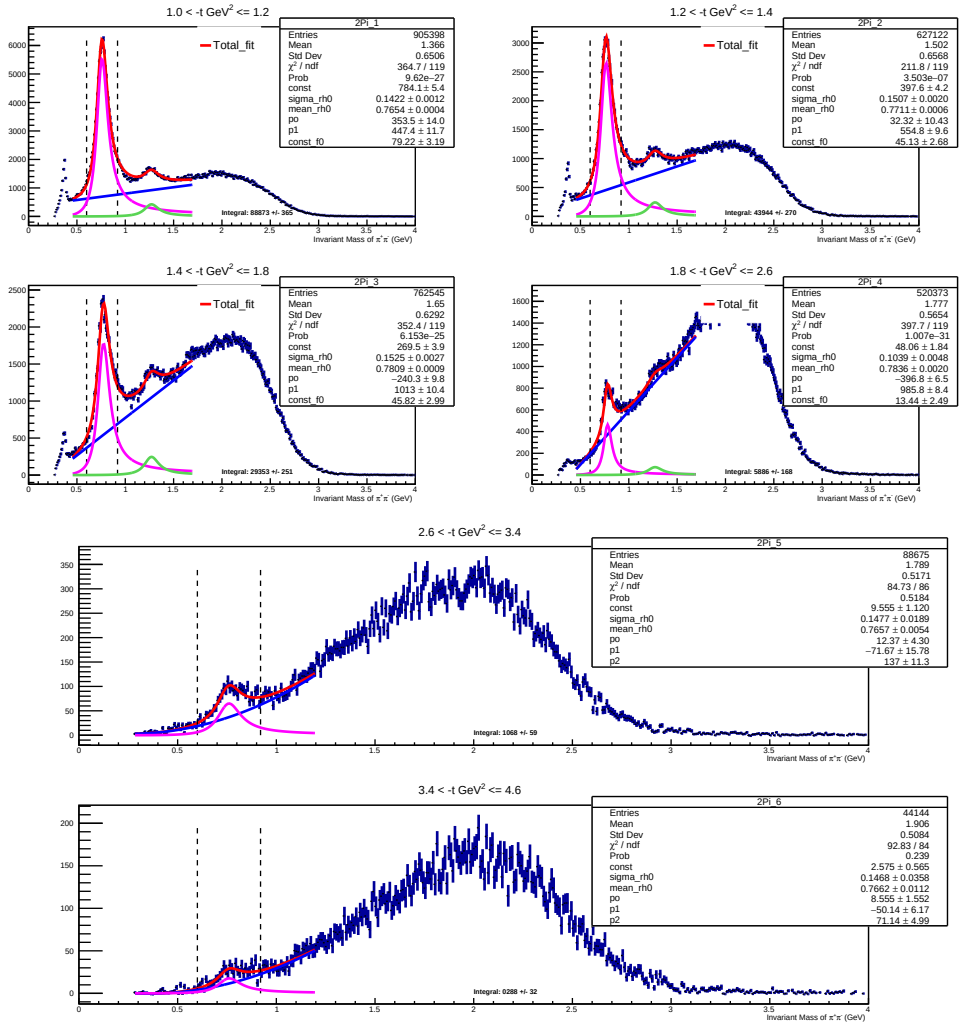

Figure 3.4: Fit to the invariant mass of $\pi^+\pi^-$ for a ^2H target with different momentum transfer $|-t|$ bins from 1 to 2.6 GeV^2. The red line represents the combined fit, the magenta line represents the signal from ρ^0 mesons, the blue line represents the first-order polynomial background, and the green line represents $f_2(1270)$ mesons with fixed width and mass. The background is modeled using a second-order polynomial for $|-t| > 2.6GeV^2$.

of $M_{\pi^+\pi^-}$ before applying any selection cuts, and after applying all selection cuts, was fitted using the relativistic Breit-Wigner function and integrated over the range of $0.6 < M_{\pi^+\pi^-} < 0.92$. This provided the ρ^0 yields for both the generated events and the reconstructed simulated events. Yield

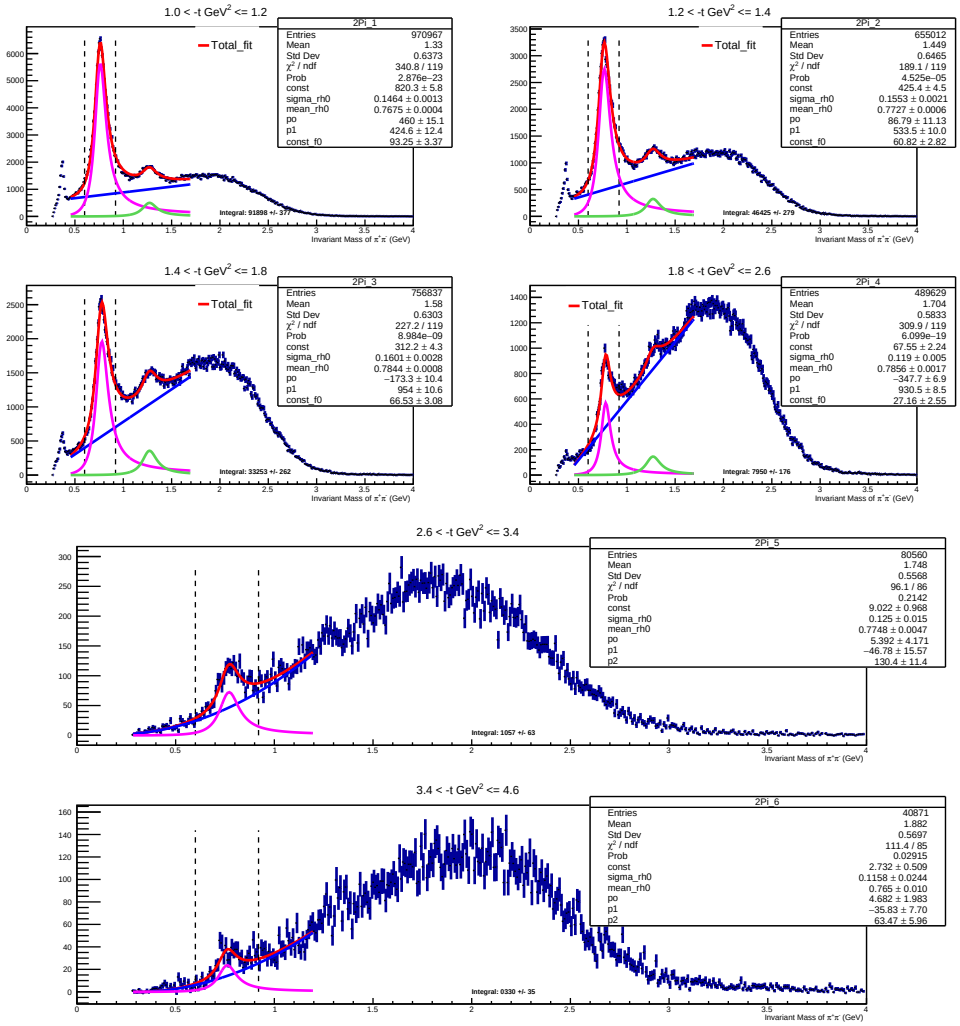

Figure 3.5: Fit to the invariant mass of $\pi^+\pi^-$ for a ^4He target with different momentum transfer $|-t|$ bins from 1 to 2.6 GeV^2. The red line represents the combined fit, the magenta line represents the signal from ρ^0 mesons, the blue line represents the first-order polynomial background, and the green line represents $f_2(1270)$ mesons with fixed width and mass. The background is modeled using a second-order polynomial for $|-t| > 2.6GeV^2$.

extracted from the fitting of invariant mass distribution over the range $0.6 < M_{\pi^+\pi^-} < 0.92$ for generated Monte Carlo events, and reconstructed (accepted) Monte Carlo events for helium target

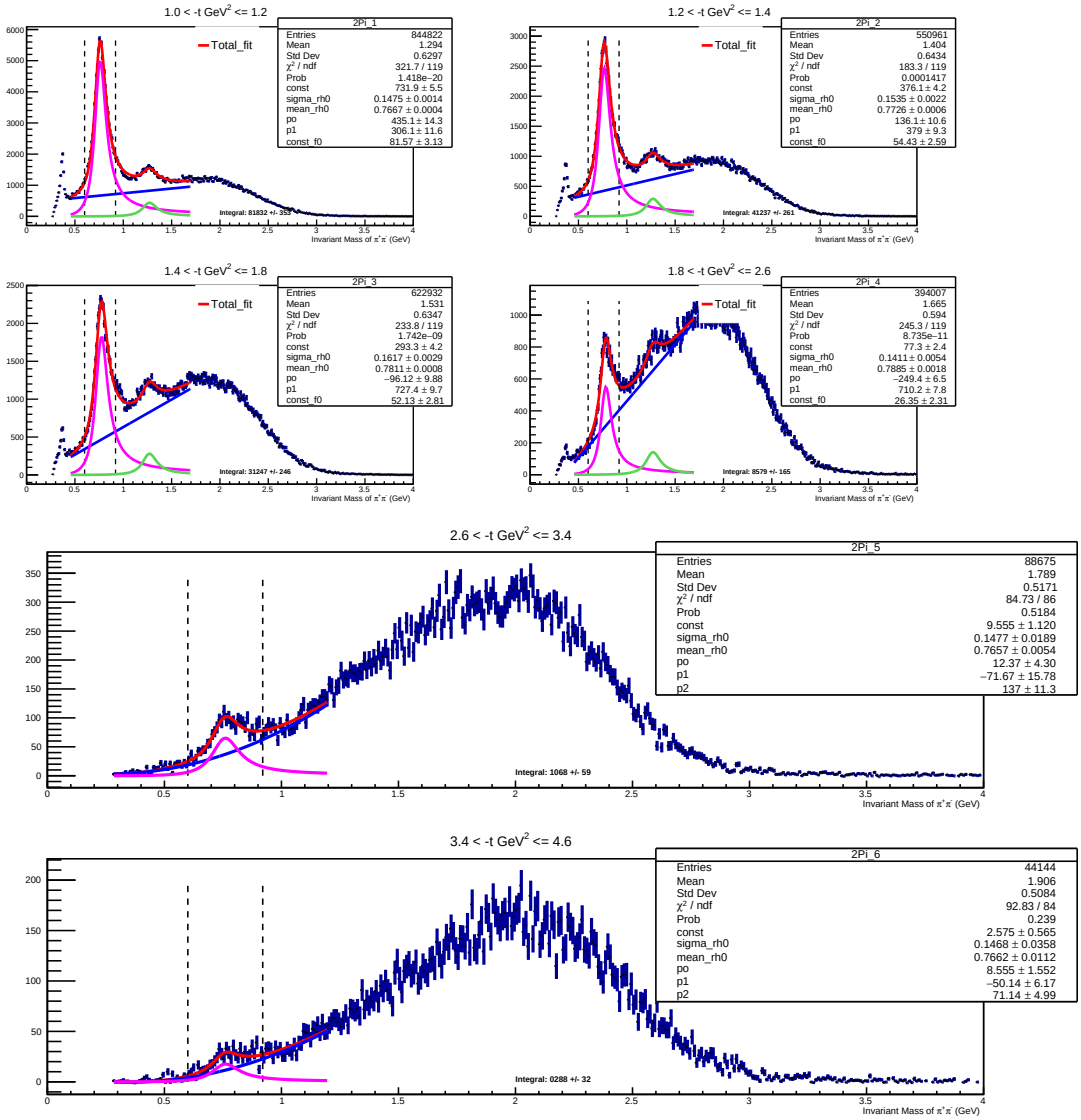

Figure 3.6: Fit to the invariant mass of $\pi^+\pi^-$ for a $^1 2C$ target with different momentum transfer $|-t|$ bins from 1 to 2.6 GeV^2. The red line represents the combined fit, the magenta line represents the signal from ρ^0 mesons, the blue line represents the first-order polynomial background, and the green line represents $f_2(1270)$ mesons with fixed width and mass. The background is modeled using a second-order polynomial for $|-t| > 2.6 GeV^2$.

Table 3.1: Yields for each nucleus as a function of momentum transfer.

Nucleus	$\lvert -t \rvert (GeV^2)$					
	1 - 1.2	1.2 - 1.4	1.4 - 1.8	1.8 - 2.6	2.6 - 3.4	3.4 - 4.6
Deuterium	88873±365	43944±270	29353±251	5886±168	1068±59	288±32
Helium	91898±377	46425±279	33253±262	7950±176	1057±63	330±35
Carbon	81832±353	41237±261	31247±246	8579±165	1051±58	357±31

are shown in Figure 3.7 and 3.8 respectively. Carbon and deuterium follow a similar distribution. The reconstructed particles satisfy all selection criteria applied to the data.

Efficiency was then calculated as the ratio of the invariant mass yield for different bins in momentum transfer $|-t|$ for reconstructed (accepted) Monte Carlo events to that of total generated Monte Carlo events. The total efficiencies for deuterium, helium, and carbon targets are shown in Figure 3.9. The efficiency for deuterium targets is observed to be slightly higher than those of helium and carbon for the given selection criteria. Additionally, the efficiency at $3.4 < |-t| GeV^2 \leq 4.6$ is less than 10% compared to the range $1.0 < |-t| GeV^2 \leq 1.2$ which is approximately 33% (deuterium target). This difference in efficiency is due to the poorer reconstruction and higher misidentification between positive pions and protons at the higher momentum transfers.

3.3 Luminosity

The photon flux was determined through the conversion of a specified fraction of the photon beam into electron-positron pairs within a thin converter, which was a part of the pair spectrometer [13]. This process reconstructs the energy of beam photons.

Luminosity was calculated using the formula,

$$\mathcal{L} = \text{flux} \times \text{Target length} \times \text{Number density} \tag{3.6}$$

where $\mathcal{L}$ is the luminosity, flux is the photon flux, and the target length and number density are specific to the target material. The target length for liquid deuterium and liquid helium was defined by the target chamber, with a value of 29.5 cm. However, for carbon multifoil, it was determined manually by the target group during assembly. The number density was calculated by multiplying Avogadro's number by the density of the target and dividing by its atomic number. More details about calculating luminosity in GlueX can be found at [46]. For this experiment, we utilized the **Lumi calculation** [1] script to calculate the tagged photon flux and luminosity.

Table 3.2 shows the measured beam photon flux and luminosity in the energy range $6.5 < E_\gamma < 10.8$ GeV.

[1] https://halldweb.jlab.org/SRC/lumi/lumi_example.pdf

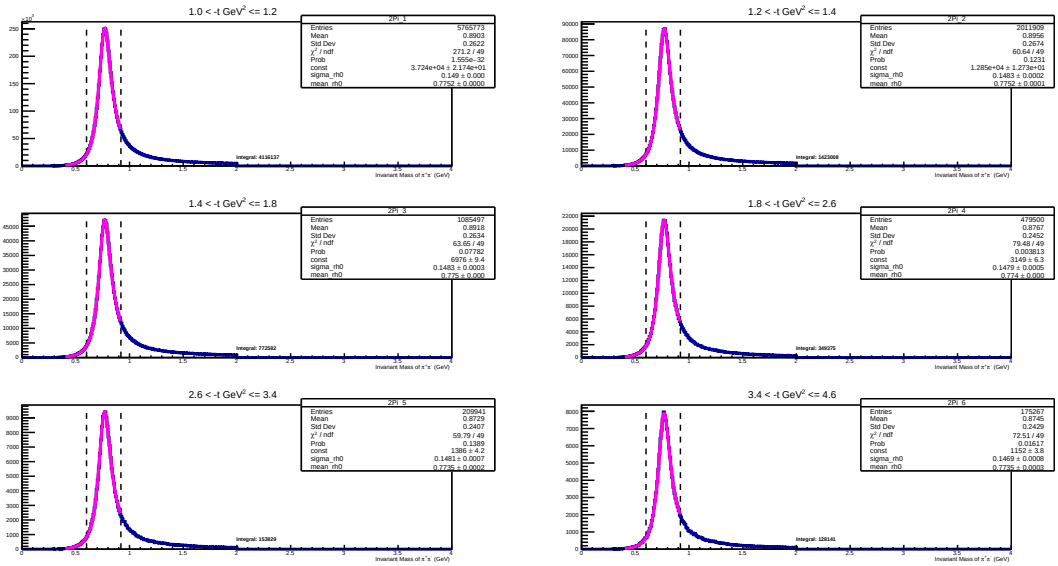

Figure 3.7: Fitting of the invariant mass distribution for generated Monte Carlo of ^4He using the relativistic Breit-Weigner function.

Nucleus	Tagged Photon Flux (10^{12})	Tagged Luminosity (pb^{-1}·nucleon)
Deuterium	13.17	33.98
Helium	30.8	63.80
Carbon	49.46	97.73

Table 3.2: Tagged flux and luminosity for each target, with beam photons having energies between 6.5 and 10.8 GeV.

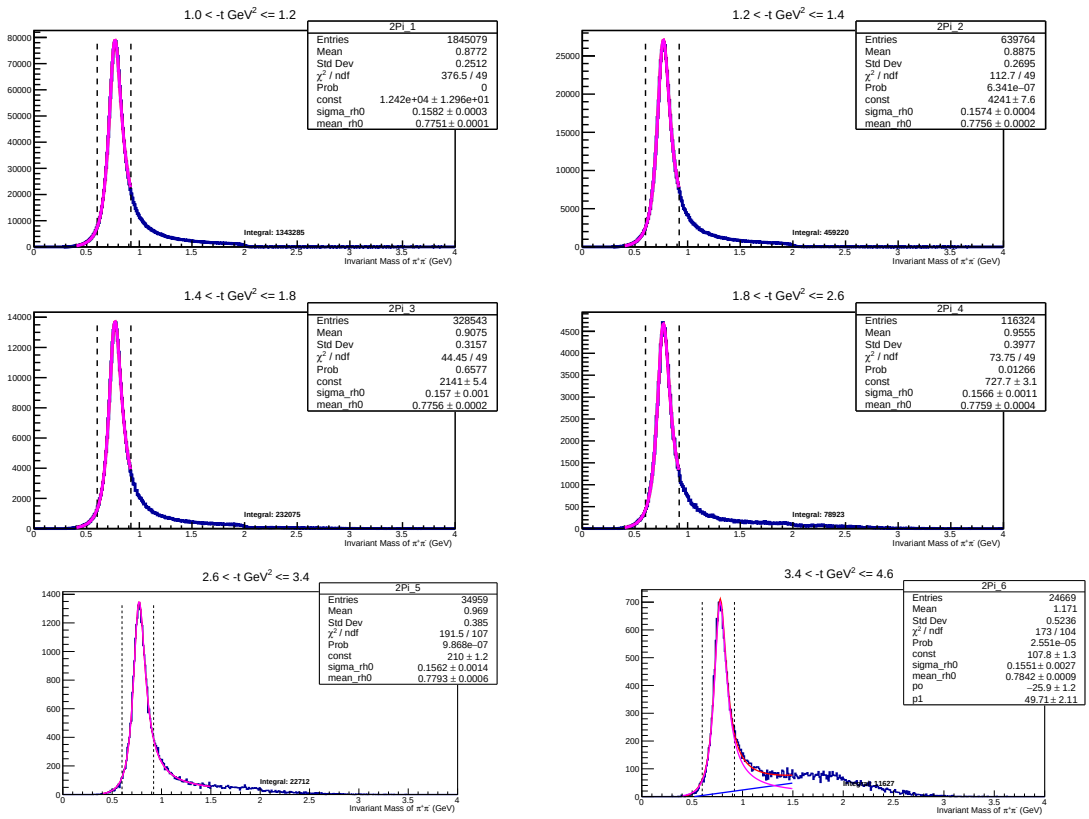

Figure 3.8: Fitting of the invariant mass distribution for reconstructed Monte Carlo of ^4He using the relativistic Breit-Weigner function. A linear polynomial order background was considered for the histogram at the bottom right.

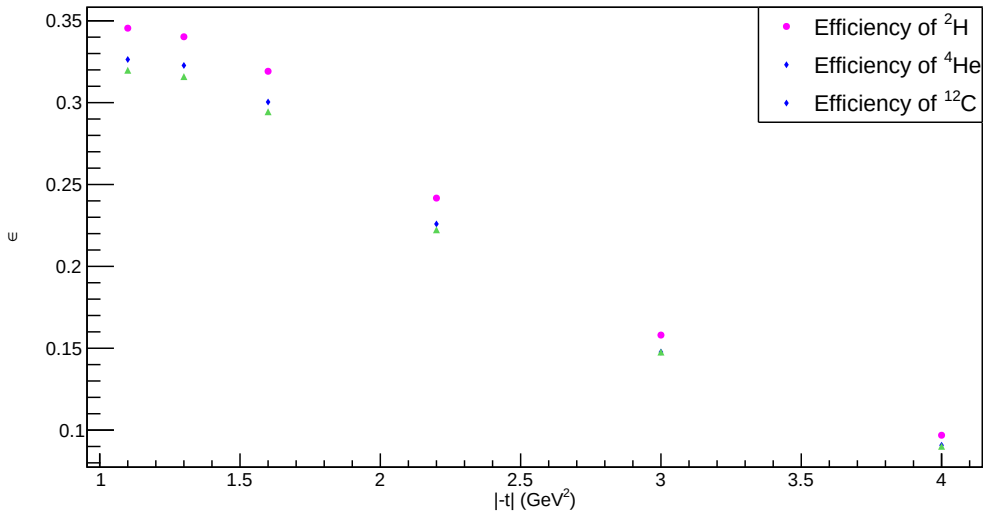

Figure 3.9: A plot of efficiency vs momentum distribution $|-t|GeV^2$.

3.4 Cross Section Extraction

The absolute cross section for the process $\gamma A \rightarrow \rho^0 pX$ was calculated using the measured γA luminosity and efficiencies derived from Monte Carlo simulations. This cross-section can be determined using the following expression:

$$\sigma = \frac{N_{signal}}{\mathcal{L} \times \epsilon \times B(\rho^0 \rightarrow \pi^+\pi^-)} \tag{3.7}$$

Here, N_{signal} represents the yield of $\rho^0 pX$ events, $\mathcal{L}$ denotes the luminosity for the nucleus in the energy range of the interest, ϵ represents the efficiency for the final states $\pi^+\pi^- p$ within the kinematics of interest, and $B(\rho^0 \rightarrow \pi^+\pi^-)$ is the branching fraction of ρ^0 decaying into $\pi^+\pi^-$ which is assumed to be 1.

3.4.1 Statistical Uncertainty in Cross-section

The statistical uncertainty for the total cross-section is given by

$$\left(\frac{\delta\sigma}{\sigma}\right)^2 = \left(\frac{\delta N_{\text{obs}}}{N_{\text{obs}}}\right)^2 + \left(\frac{\delta\mathcal{L}}{\mathcal{L}}\right)^2 + \left(\frac{\delta\epsilon}{\epsilon}\right)^2 \tag{3.8}$$

Given that the branching fraction $B(\rho^0 \rightarrow \pi^+\pi^-)$ is assumed to be 1, it doesn't contribute to the uncertainty. So, the statistical uncertainty in the cross-section is determined by the uncertainty in the yield, luminosity, and efficiency. For this preliminary study, we consider only the uncertainty from the yields.

3.5 Nuclear Transparency

Nuclear Transparency for Helium and Carbon targets is evaluated as follows:

$$\begin{aligned} T(^4\text{He}) &= \frac{\sigma_{(^4\text{He})}}{\sigma_{(^2\text{H})}} \\ T(^{12}\text{C}) &= \frac{\sigma_{(^{12}\text{C})}}{\sigma_{(^2\text{H})}} \end{aligned} \tag{3.9}$$

3.5.1 Statistical Uncertainty in Nuclear Transparency

The statistical uncertainty for nuclear transparency is given as

$$\left(\frac{\delta T}{T}\right)^2 = \left(\frac{\delta\sigma_{\text{A}}}{\sigma_{\text{A}}}\right)^2 + \left(\frac{\delta\sigma d}{\sigma d}\right)^2 \tag{3.10}$$

where σ_A and σ_d represents the cross-section of nuclei targets and deuterium.

3.6 Preliminary Results

The Preliminary absolute cross section using only the statistical uncertainty from yields for deuterium, helium, and carbon is shown in Figure 3.10. Additionally, nuclear transparency (T) as a function of momentum transfer for both helium and carbon is also shown in Figure 3.11.

3.7 Future Works

In our analysis of nuclear transparency for the process $\gamma A \rightarrow \rho^0 pX$ using liquid helium, deuterium, and carbon targets. The uncertainties in the cross-section were solely based on the data yields, extracted from fits to the background using a polynomial function. We intend to perform a more rigorous study of the backgrounds in the near future. For the future effort, I will explore the following:

1. Study the background of the data by using the background model simulation from GlueX.

2. Work on systematic uncertainties associated with the cross-section ratio.

3. To calculate photon transparency to look for the transition of photon from vector meson to that of point like configuration.

4. Study the onset of CT by comparing against theoretical calculations

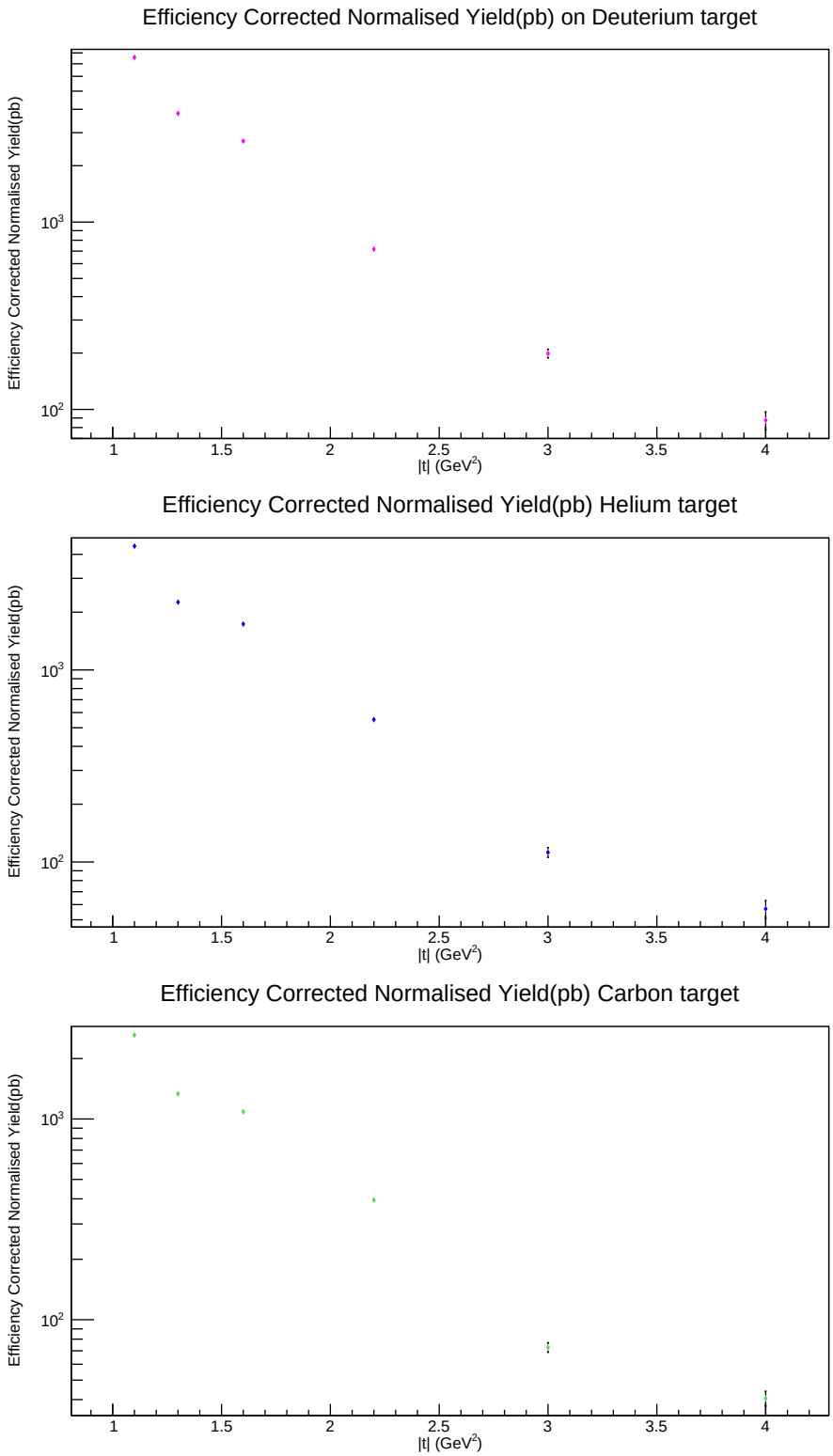

Figure 3.10: Cross section for $\rho^0 \rightarrow \pi^+\pi^-$ for Deuterium(top), Helium(middle), and Carbon(bottom) $|-t|$ from 1.0 to 4.6 GeV^2

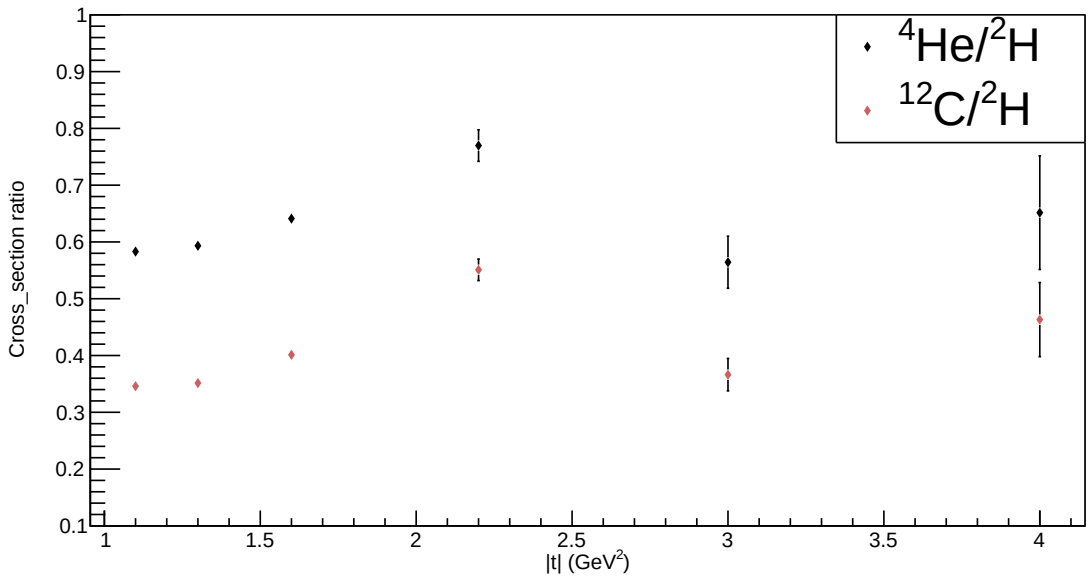

Figure 3.11: Nuclear Transparency as a function of momentum transfer. For this extraction, only statistical uncertainties from data yield were considered.

REFERENCES

[1] "Analyzing Physics Reactions with the ReactionFilter Plugin in JLab,", https://halldweb.jlab.org/wiki/index.php/ReactionFilter. 9

[2] "GlueX Collaboration: Spring 2017 Analysis Launch Cuts,", https://halldweb.jlab.org/wiki/index.php/Spring_2017_Analysis_Launch_Cuts. 9

[3] "JLab Data Acquisition Group, CODA Online Data Formats.,", https://coda.jlab.org/drupal/system/files/eventbuilding.pdf. 8

[4] "Physics Analysis Root Tree in JLab Hall D,", https://halldweb.jlab.org/wiki/index.php/Analysis_TTreeFormat. 9

[5] "Mattione, P. Least Squares Kinematic Fitting of Physics Reactions.,", 2006, https://halldweb.jlab.org/DocDB/0021/002112/005/KinematicFitting.pdf. 12, 13

[6] "Jefferson Lab CCDB Wiki,", 2019, https://github.com/JeffersonLab/ccdb/wiki. 8

[7] "DSelector,", 2022. 8

[8] D. Abbott et al., "Quasifree $(e, e'p)$ reactions and proton propagation in nuclei," *Phys. Rev. Lett.*, vol. 80, 1998, pp. 5072–5076, https://doi.org/10.1103/PhysRevLett.80.5072. 4

[9] J. Aclander et al., "Nuclear transparency in $90^{\circ}_{\text{c.m.}}$ quasielastic $A(p, 2p)$ reactions," *Phys. Rev. C*, vol. 70, Jul 2004, p. 015208. 3

[10] S. Adhikari et al., "The GlueX beamline and detector," *Nuclear Instruments and Methods in Physics Research Section A: Accelerators, Spectrometers, Detectors and Associated Equipment*, vol. 987, 2021, p. 164807, https://www.sciencedirect.com/science/article/pii/S0168900220312043. 6, 7

[11] J. S. G. V. Alexander Austregesilo, Dave Mack, "Gluex Collaboration Task Force Report:Vertex Recoil Proton Event Selection,", 2021, https://halldweb.jlab.org/DocDB/0049/004924/002/TaskForce_ProtonFiducialVertex.pdf. 16

[12] Ballard et al., "Refurbishment and testing of the 1970's era LASS solenoid coils for Jlab's Hall D," *AIP Conference Proceedings*, vol. 1434, no. 1, 06 2012, pp. 861–868, https://doi.org/10.1063/1.4707001. 7

[13] F. Barbosa et al., "Pair spectrometer hodoscope for Hall D at Jefferson Lab," *Nuclear Instruments and Methods in Physics Research Section A: Accelerators, Spectrometers, Detectors and Associated Equipment*, vol. 795, 2015, pp. 376–380, https://doi.org/10.1016/j.nima.2015.06.012. 6, 27

[14] T. Beattie et al., "Construction and performance of the barrel electromagnetic calorimeter for the GlueX experiment," *Nuclear Instruments and Methods in Physics Research Section A: Accelerators, Spectrometers, Detectors and Associated Equipment*, vol. 896, 2018, pp. 24–42, https://doi.org/10.1016/j.nima.2018.04.006. 7

[15] D. Bhetuwal et al., "Ruling out Color Transparency in Quasielastic ^{12}C(e, e'p) up to Q^2 of 14.2 $(\mathrm{GeV/c})^2$," *Phys. Rev. Lett.*, vol. 126, Feb 2021, p. 082301, https://link.aps.org/doi/10.1103/PhysRevLett.126.082301. 4

[16] B. Blattel et al., ," *Phys. Rev. Lett.*, vol. 70, 1993, p. 896. 4

[17] S. J. Brodsky and G. F. de Teramond, "Spin Correlations, QCD Color Transparency, and Heavy-Quark Thresholds in Proton-Proton Scattering," *Phys. Rev. Lett.*, vol. 60, May 1988, pp. 1924–1927. 4

[18] S. J. Brodsky and A. Mueller, "Using nuclei to probe hadronization in QCD," *Physics Letters B*, vol. 206, no. 4, 1988, pp. 685–690, https://www.sciencedirect.com/science/article/pii/0370269388907198. 1

[19] J. Carlson et al., "Quantum Monte Carlo methods for nuclear physics," *Rev. Mod. Phys.*, vol. 87, Sep 2015, pp. 1067–1118. 1

[20] A. Carroll et al., "Nuclear Transparency to Large Angle p p Elastic Scattering," *Phys. Rev. Lett.*, vol. 61, 1988, pp. 1698–1701. 3

[21] B. Clasie et al., "Measurement of Nuclear Transparency for the $A(e, e'\pi^+)$ Reaction," *Phys. Rev. Lett.*, vol. 99, Dec 2007, p. 242502. 4

[22] M. Dugger et al., "Design and construction of a high-energy photon polarimeter," *Nuclear Instruments and Methods in Physics Research Section A: Accelerators, Spectrometers, Detectors and Associated Equipment*, vol. 867, 2017, pp. 115–127, https://doi.org/10.1016/j.nima.2017.05.026. 6

[23] D. Dutta, K. Hafidi, and M. Strikman, "Color Transparency: past, present and future," *Prog. Part. Nucl. Phys.*, vol. 69, 2013, pp. 1–27. 2

[24] D. Dutta, F. Xiong, L. Zhu, J. Arrington, T. Averett, E. Beise, J. Calarco, T. Chang, J. P. Chen, E. Chudakov, et al., "Nuclear transparency with the $\gamma n \longrightarrow \pi^- p$ process in ^4He," *Physical Review C*, vol. 68, no. 2, 2003, p. 021001. 4, 5

[25] L. El Fassi et al., "Evidence for the onset of color transparency in ρ^0 electroproduction off nuclei," *Phys. Lett. B*, vol. 712, 2012, pp. 326–330. 4

[26] L. Frankfurt, G. Miller, and M. Strikman, "Color transparency phenomenon and nuclear physics," *Comments Nucl.Part.Phys.*, vol. 21, no. 1, 1992, pp. 1–39. 2

[27] K. Garrow et al., "Nuclear transparency from quasielastic $A(e,e'p)$ reactions up to $Q^2 = 8.1\ (GeV/c)^2$," *Phys. Rev. C*, vol. 66, 2002, p. 044613. 4

[28] R. Glauber, *Lectures in Theoretical Physics ed W E Brittin*, vol. I, Interscience, New York, 1959. 1

[29] N. Jarvis et al., "The Central Drift Chamber for GlueX," *Nuclear Instruments and Methods in Physics Research Section A: Accelerators, Spectrometers, Detectors and Associated Equipment*, vol. 962, 2020, p. 163727, https://www.sciencedirect.com/science/article/pii/S0168900220302771. 7

[30] B. Kundu et al., "Perturbative color transparency in electroproduction experiments," *Phys. Rev. D*, vol. 62, Nov 2000, p. 113009. 4

[31] A. Larionov and M. Strikman, "Exploring QCD dynamics in medium energy γA semiexclusive collisions," *Physics Letters B*, vol. 760, 2016, pp. 753–758, https://doi.org/10.1016/j.physletb.2016.07.067. 3, 6, 15

[32] A. Leksanov et al., "Energy dependence of nuclear transparency in $^{12}C(p,2p)$ scattering," *Phys.Rev.Lett.*, vol. 87, 2001, p. 212301. 3

[33] N. Makins et al., "Momentum transfer dependence of nuclear transparency from the quasielastic $^{12}C(e,e'p)$ reaction," *Phys. Rev. Lett.*, vol. 72, 1994, pp. 1986–1989. 4

[34] I. Mardor et al., "Nuclear transparency in large momentum transfer quasielastic scattering," *Phys. Rev. Lett.*, vol. 81, 1998, pp. 5085–5088. 3

[35] H. Marukyan et al., "Studying Short-Range Correlations with Real Photon Beams at GlueX," https://www.jlab.org/exp_prog/proposals/19/PR12-19-003.pdf, 2020. 6

[36] K. Moriya, J. Leckey, M. Shepherd, K. Bauer, D. Bennett, H. Egiyan, J. Frye, J. Gonzalez, S. Henderson, D. Lawrence, R. Mitchell, E. Smith, P. Smith, and A. Somov, "A measurement of the energy and timing resolution of the GlueX Forward Calorimeter using an electron beam," *Nuclear Instruments and Methods in Physics Research Section A: Accelerators, Spectrometers, Detectors and Associated Equipment*, vol. 726, 2013, pp. 60–66, https://doi.org/10.1016/j.nima.2013.05.109. 7

[37] A. H. Mueller, ," *Proceedings of the Seventeenth Recontre de Moriond Conference on Elementary Particle Physics*, Les Arcs, France, 1983. 2

[38] T. O'Neill et al., "A-dependence of nuclear transparency in quasielastic $A(e,e'p)$ at high Q^2," *Phys. Lett. B*, vol. 351, 1995, pp. 87–92. 4

[39] B. Z. others, "TOF detector description for CDR,", 2008, https://halldweb.jlab.org/DocDB/0009/000994/004/TOF_cdr.pdf. 7

[40] L. Pentchev et al., "Studies with cathode drift chambers for the GlueX experiment at Jefferson Lab," *Nuclear Instruments and Methods in Physics Research Section A: Accelerators, Spectrometers, Detectors and Associated Equipment*, vol. 845, 2017, pp. 281–284, https://www.sciencedirect.com/science/articlepii/S0168900216302893. 7

[41] E. Pooser et al., "The GlueX Start Counter Detector," *Nuclear Instruments and Methods in Physics Research Section A: Accelerators, Spectrometers, Detectors and Associated Equipment*, vol. 927, 2019, pp. 330–342, https://www.sciencedirect.com/science/article/pii/S0168900219302128. 7

[42] X. Qian et al., "Experimental study of the $A(e,e'\pi^+)$ reaction on ^{1}H, ^{2}H, ^{12}C, ^{27}Al, ^{63}Cu, and ^{197}Au," *Phys. Rev. C*, vol. 81, May 2010, p. 055209. 4

[43] U. Timm, "Coherent bremsstrahlung of electrons in crystals," *Fortsch. Phys.*, vol. 17, 1969, pp. 765–808, https://doi.org/10.1002/prop.19690171202. 6

[44] R. L. Workman and Others, "Review of Particle Physics," *PTEP*, vol. 2022, 2022, p. 083C01, https://doi.org/10.1093/ptep/ptac097. 8

[45] G. L. Yang et al., "A summary of the optics design for the GlueX single dipole tagger spectrometer,", 2009, https://halldweb.jlab.org/doc-public/DocDB/ShowDocument?docid=1186. 6

[46] J. Zarling, "Extracting cross sections: Luminosity,Branching Fractions, and Efficiency: GlueX, Workshop 2022,", 2008, https://halldweb.jlab.org/DocDB/0055/005598/003/GlueX_May2022_flux_efficiency_xsec_workshop.pdf. 28